Chinese Chemical Letters 34 (2023) 107756

Contents lists available at ScienceDirect

Chinese Chemical Letters

journal homepage: www.elsevier.com/locate/cclet

Leather waste as precursor to prepare bifunctional catalyst for alkaline and neutral zinc-air batteries

Zeyu Zhu[a,1], Jing Zhu[a,1], Yangshen Chen[a,1], Xinxin Liu[a], Mengchun Zhang[b], Mengxiao Yang[a], Mengyu Liu[b], Jiansheng Wu[a,*], Sheng Li[a,*], Fengwei Huo[a,*]

[a] Key Laboratory of Flexible Electronics (KLOFE), Institute of Advanced Materials (IAM), Nanjing Tech University, Nanjing 211816, China
[b] School of Chemistry and Molecular Engineering, Nanjing Tech University, Nanjing 211816, China

ARTICLE INFO

Article history:
Received 6 May 2022
Revised 26 May 2022
Accepted 16 August 2022
Available online 19 August 2022

Keywords:
Leather waste
Zinc-air batteries
Bifunctional electrocatalyst
FeNi alloy
Biomass

ABSTRACT

Carbon materials derived from biomass waste are considered as potential electrocatalysts for applications in zinc-air batteries (ZABs) due to their low cost and good catalytic activity. Here, we reported the preparation of gel-based catalysts through utilizing hydrolyzed waste leather powder cross-linked with metallic salt solutions. After calcination, iron-nickel alloy anchored in nitrogen-doped porous carbon catalysts (FeNi@NDC) was achieved. Compared with commercial Pt/C catalyst, FeNi@NDC-800 exhibited lower $E_{1/2}$ (0.77 V) and better durability. More importantly, the resulting FeNi@NDC-800-based alkaline ZABs achieved power density of 93.01 mW/cm^2 and open circuit voltage of 1.45 V, which the FeNi@NDC-800-based neutral ZAB displayed a charge/discharge cycle stability of 275 h. This work opens up the possibility of rational design and preparation of low-cost and high-performance electrocatalysts from recyclable leather waste.

Biomass materials have been used as potential precursor materials for bifunctional catalysts as an alternative to precious metals because they are rich in carbon and other heteroatoms (such as N, P, S), low cost, readily available, renewable, sustainable, and environmentally friendly [1,2]. Among them, leather has attracted renewed interest due to its huge global consumer market with global leather production of approximately 4.8 billion square feet [3]. However, in the traditional tanning process, only 20% of the raw leather can be converted into leather products, leading to a large amount of solid leather waste and posing great damage to the environment [4,5]. Therefore, efficient utilization of solid leather waste as precursor for the preparation of nitrogen-doped porous carbon is of great importance to the environmental and energy fields [6,7].

Zinc-air batteries (ZABs) are widely considered as the next-generation clean energy storage devices due to their high energy density (1086 Wh/kg), low cost, and good safety [8–10]. At present, great progress has been achieved in the study of ZABs in alkaline but the alkaline electrolyte usually reacts with CO_2 in the air to form carbonates during practical operation since ZABs are semi-open, thus blocking the gas diffusion layer, reducing the ionic conductivity of the solution, and greatly reducing the lifetime of the ZABs [11,12]. To alleviate these problems, ZABs with neutral electrolytes have attracted attention as a viable alternative to alkaline ZABs [13]. Unfortunately, due to the low OH^- concentration, the oxygen reduction reaction (ORR) and oxygen evolution reaction (OER) performances of the electrocatalyst in neutral electrolytes are less satisfactory than those of the alkaline electrolytes [14]. Current efforts are focused on carbon-loaded platinum nanoparticles (Pt/C) as the most efficient catalysts for neutral electrolytes due to their high catalytic activity for ORR [15]. However, the application of Pt/C catalysts in neutral ZABs is limited by their high cost, insufficient stability and poor catalytic performance for OER [16]. Therefore, developing non-precious metal-based bifunctional catalysts with high efficiency, low cost and robustness for neutral ZABs has become an urgent priority, there are already many materials used in this field [17–22].

Leather waste is rich in natural collagen with abundant functional groups, and gel materials can be prepared through coordinating metal Fe^{3+} with surface functional groups [23]. Herein, we present a strategy to form gels by cross-linking metallic Fe^{3+} and Ni^{2+} with leather powder, and then prepare a nitrogen-doped porous carbon active material (FeNi@NDC) of the iron-nickel alloy after carbonization. Specifically, the collagen in the leather powder coordinates with Fe^{3+} to form a gel cross-linked network,

* Corresponding authors.
E-mail addresses: iamjswu@njtech.edu.cn (J. Wu), iamsli@njtech.edu.cn (S. Li), iamfwhuo@njtech.edu.cn (F. Huo).
[1] These authors contributed equally to this work.

https://doi.org/10.1016/j.cclet.2022.107756
1001-8417/

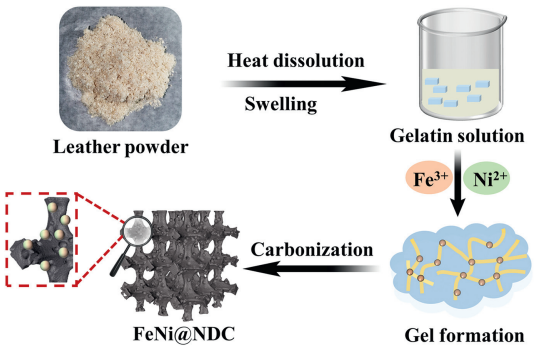

Scheme 1. Schematic illustration of the fabrication process of FeNi@NDC.

which facilitates the immobilization of metal nanoparticles. The subsequent carbonization process promotes the formation of homogeneous FeNi alloy nanoparticles on the carbon substrate. Notably, the FeNi@NDC catalyst exhibits excellent electrocatalytic performance ($E_{1/2}$ = 0.77 V and overpotential at 10 mA/cm^2 = 1.62 V) and stability in both alkaline and neutral electrolytes, offering a promising prospect to replace noble metal catalysts. In addition, neutral ZABs assembled with FeNi@NDC as catalysts have a high power density (31.44 mW/cm^2) and maintain long charge/discharge cycle stability (275 h). This strategy is expected to advance the development of safe neutral flexible ZABs in the future.

The synthetic process of FeNi@NDC catalyst is shown in Scheme 1. Firstly, the leather powder was heated and dissolved in deionized water, and then Fe^{3+} and Ni^{2+} were added to form a gel by ligand interaction with the functional groups in the leather powder. The gel was formed after rapid stirring to promote the uniform distribution of bimetallic FeNi ions in the carbon precursor. The samples were freeze-dried to remove the moisture, and then heat-treated continuously at 5 °C/min to 800 °C for 2 h. After the carbonization process, dispersed carbon particles were formed as shown in Fig. S1 (Supporting information), FeNi nanoparticles were found to anchor on nitrogen-doped porous carbon, and Fe@NDC was obtained. As shown in Figs. S2 and S3 (Supporting information), Fe and Ni account for five percent of Fe@NDC, with a mass ratio of about 1:1. Similarly, FeCo@NDC and Fe@NDC were prepared by the similar synthetic processes.

Transmission electron microscope (TEM) is used to identify the surface morphology and structure of the FeNi@NDC. As shown in Fig. S4a (Supporting information), after the carbonization process, the leather powder cross-linked with Fe and Ni ions in the gel material form spherical bimetallic nanoparticles dispersed in a nitrogen-doped carbon matrix. The high-resolution TEM (HRTEM) image of FeNi@NDC in Fig. S4b (Supporting information) exhibits a clear lattice stripe of 0.208 nm, which corresponds to the (111) crystal plane of $Fe_{0.64}Ni_{0.36}$. The corresponding elemental spectra further demonstrate the uniform distribution of C and N in the catalyst, with Fe and Ni elements locating mainly in the bimetal nanoparticles (Figs. S4c–g in Supporting information). These metal nanoparticles encapsulated in graphite carbon can effectively avoid agglomeration or exfoliation under highly carbonization conditions [24].

Fig. 1a shows the X-ray diffraction (XRD) pattern of FeNi@NDC, where the broad diffraction peak at ≈23° is related to the (002) crystal plane of the graphite carbon originating from the porous carbon, a result of leather carbonization. Other diffraction peaks at 43.60°, 50.79° and 74.68° are consistent with the (111), (200) and (220) crystal planes of $Fe_{0.64}Ni_{0.36}$ (JCPDS No. 47-1405). Additional comparison samples XRD are shown in Fig. S5a. The Raman spectra of the three samples in Fig. S5b exhibit two distinct peaks at approximately 1350 and 1580 cm^{-1}, corresponding to the D and

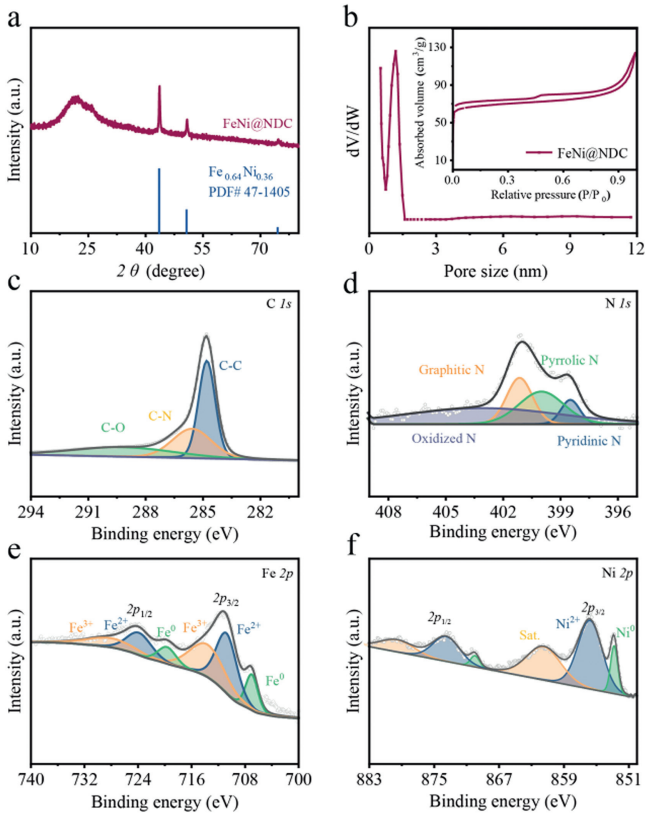

Fig. 1. Compositional characterization of FeNi@NDC. (a) XRD spectra of FeNi@NDC. (b) N_2 sorption isotherms and pore size distribution of FeNi@NDC. XPS of FeNi@NDC (c) C 1s, (d) N 1s, (e) Fe 2p and (f) Ni 2p.

G bands of carbon materials, respectively. FeNi@NDC has a higher I_G/I_D value compared to Fe@NDC and FeCo@NDC, reflecting that the higher degree of graphitization contributes to the conductivity of catalysts. The N_2 adsorption isotherm is used to test the specific surface area and pore size distribution of FeNi@NDC (Fig. 1b), exhibiting a high specific surface area of ~266.9 m^2/g (calculated by the Brunauer–Emmett–Teller method). The pore width distribution reveals a large number of micropores in FeNi@NDC, which can accommodate a large number of ORR/OER active sites [25]. Oxygen molecules can be trapped by micropores, allowing them to bind more efficiently to catalytic active sites, which in turn promote catalytic activity [8,26].

X-ray photoelectron spectroscopy (XPS) is used to determine the elemental composition and valence states of the prepared FeNi@NDC composite. The presence of five elements: Fe, Ni, C, O and N is evidenced by Fig. S6 (Supporting information). As shown in the C 1s spectrum of the FeNi@NDC composites (Fig. 1c), three distinguishable peaks are identified at 284.8, 285.6 and 289.8 eV, which are assigned to the binding energies of the C–C, C–N and C–O groups, respectively. The N 1s spectrum in Fig. 1d can be deconvoluted into three component peaks of pyridinic N (398.5 eV), pyrrolic N (399.9 eV) and graphitic N (401.1 eV). Among these, pyridine N can be utilized as an active ingredient to modify the structure of the local electrons, and improve surface wettability [27], which would favor electrochemical processes. The high-resolution spectrum of Fe 2p in Fig. 1e shows the two bands at 707.1 and 719.9 eV, which corresponds to zero-valence state Fe. The two bands at 711.0 and 724.2 eV are attributed to Fe^{2+} species, and the other two bands at 714.3 and 728.9 eV are attributed to Fe^{3+} species, possibly due to the oxidation of the surface of the metal alloy. The zero-valence state (Fe^0) of Fe in the Fe 2p spectrum corresponds to the metallic Fe in the FeNi alloy [28]. In addi-

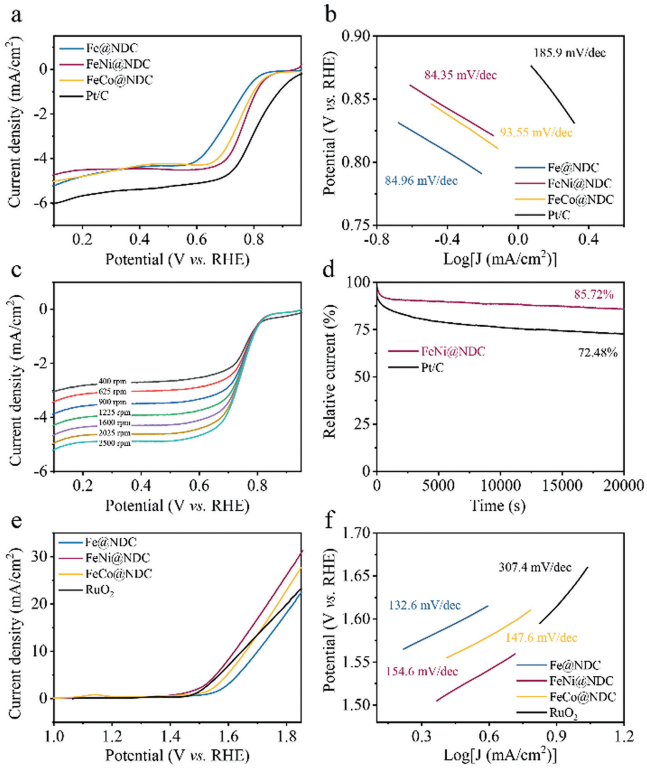

Fig. 2. Electrochemical characterization of the catalysts. (a, b) ORR polarization curves in O_2-saturated 0.1 mol/L KOH solution at a rotation speed of 1600 rpm and the corresponding Tafel plots of FeNi@NDC, FeCo@NDC, Fe@NDC and Pt/C. (c) LSV curves of FeNi@NDC for ORR at various rotation speeds. (d) ORR chronoamperometry response of FeNi@NDC. (e, f) OER curves in O_2-saturated 0.1 mol/L KOH solution at a rotating speed of 1600 rpm and the corresponding Tafel plots of FeNi@NDC, FeCo@NDC, Fe@NDC and RuO_2.

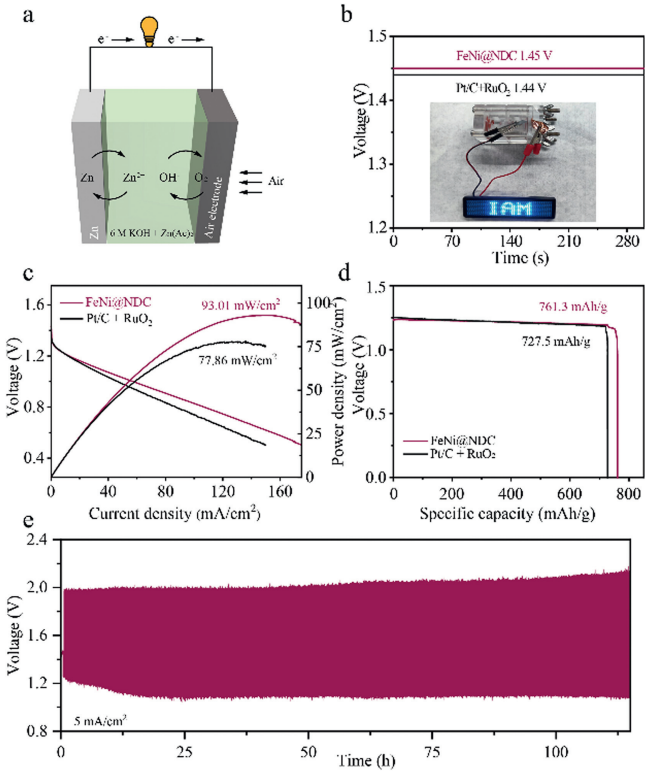

Fig. 3. ZAB performance of FeNi@NDC. (a) Schematic illustration of the alkaline liquid ZAB. (b) OCV plots of the alkaline liquid ZAB. (c) Discharging polarization curves and corresponding power density plots. (d) Discharge specific capacity curve at 10 mA/cm^2. (e) Charge/discharge cycle stability of liquid ZAB based on FeNi@NDC at 5 mA/cm^2.

tion, the high resolution of the Ni 2p spectrum can be divided into Ni $2p_{1/2}$ and Ni $2p_{3/2}$ (Fig. 1f). The peak at 852.8 eV corresponds to the metallic state of nickel, while peak at 855.9 eV is attributed to Ni $2p_{3/2}$ of Ni^{2+} [29–31]. These results demonstrate the successful incorporation of FeNi metal alloy nano particles into N-doped porous carbon, which demonstrates good catalytic performance in the ORR and OER. Such composites prevent the dissolution, corrosion and aggregation of alloy catalysts, improve electrical conductivity, facilitate electrolyte penetration, and provides fast reaction kinetics through strong coupling with the alloy [31].

To illustrate the electrocatalytic activity of FeNi@NDC, the cyclic voltammetry (CV) was tested in N_2- or O_2-saturated 0.1 mol/L KOH solution. Compared with the curves in Fig. S7, a significant peak at 0.7 V is observed in the O_2-saturated solution, indicating the ORR electrocatalytic potential of FeNi@NDC, while no obvious peak is found in the N_2-saturated solution. The LSV curves of FeNi@NDC, FeCo@NDC, Fe@NDC, and 20 wt% Pt/C are shown in Fig. 2a. The half-wave potential ($E_{1/2}$) of FeNi@NDC is 0.77 V, which is close to that of the 20 wt% Pt/C ($E_{1/2}$, 0.82 V) and higher than that of FeCo@NDC ($E_{1/2}$, 0.74 V) and Fe@NDC ($E_{1/2}$, 0.70 V). This advantage indicates that FeNi@NDC has good electrocatalytic activity for ORR. The Tafel curves of different samples are shown in Fig. 2b. FeNi@NDC (84.35 mV/dec) has a lower Tafel slope than 20 wt% Pt/C (185.9 mV/dec), suggesting its good catalytic kinetics. To further analyze the ORR reaction mechanism of FeNi@NDC catalysts, LSV curves at different rotational speeds from 400 rpm to 2500 rpm were tested to determine the number of electron transfer (Fig. 2c). According to the Koutecky–Levich equation, there are 4 electrons transferred (Fig. S8 in Supporting information), which is consistent with the reaction kinetic results, indicating a high $4e^-$ selectivity out of FeNi@NDC catalyst. The stability of FeCo@NDC can be tested by using the chronoamperometric response. As shown in Fig. 2d, 85.72% of the initial ORR current is retained at 0.7 V after 20000 s, which is superior than that of Pt/C (72.48%). The OER electrocatalytic performances of FeNi@NDC, FeCo@NDC, Fe@NDC and RuO_2 are investigated in detail (Fig. 2e). Specifically, the FeNi@NDC catalyst generates a current density of 10 mA/cm^2 at a potential ($E_{j=10}$) of 1.62 V, which is identical to that of RuO_2 ($E_{j\ =\ 10} = 1.65$ V) and lower than that of FeCo@NDC ($E_{j\ =\ 10} = 1.66$ V) and Fe@NDC ($E_{j\ =\ 10} = 1.70$ V). This comparable OER performance of FeNi@NDC is further confirmed by the Tafel plots in Fig. 2f showing its lower Tafel slope (154.6 mV/dec) than RuO_2 (307.4 mV/dec). The bifunctional catalytic activity of FeNi@NDC should be attributed to the synergistic effect of alloy particles and nitrogen-doped carbon substrate [32–34].

Due to the above electrocatalytic properties, an alkaline liquid ZAB is assembled by using the FeNi@NDC catalyst. As shown in Fig. 3a, polished zinc foil is used as the anode, FeNi@NDC is the air electrode, and 6 mol/L KOH and 0.2 mol/L $Zn(Ac)_2$ are the electrolyte. Pt/C + RuO_2 (1:1) batteries assembled in the same way are used as reference. The open-circuit voltages (OCVs) of the ZABs of FeNi@NDC and Pt/C + RuO_2 were tested (Fig. 3b). Both batteries demonstrate stable OCV performance with negligible differences (FeNi@NDC 1.45 V, and Pt/C + RuO_2 1.44 V). Subsequently, FeNi@NDC ZAB is used as a power source to light up a screen with blue LED bulbs. The rate capability of the FeNi@NDC-based ZABs was also explored by discharging at different current densities of 1, 2, 5 and 10 mA/cm^2. As shown in Fig. S9 (Supporting information), the voltage of the ZABs using FeNi@NDC decreases by 0.12 V relative to the initial value when the current density is switched to 1 mA/cm^2, which indicates its good stability and re-

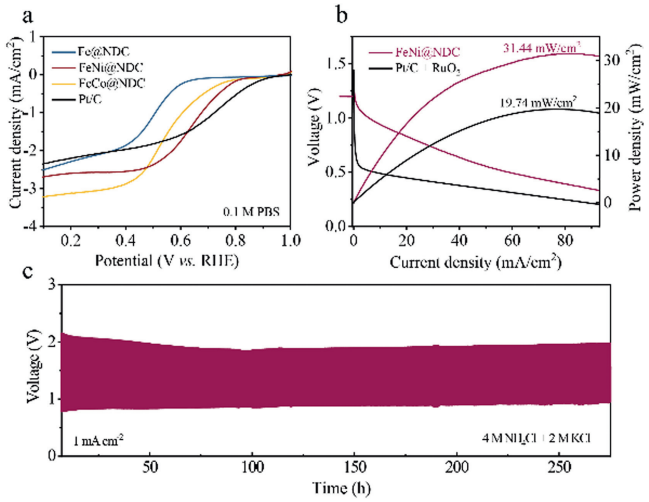

Fig. 4. (a) ORR polarization curves in O_2-saturated 0.1 mol/L PBS solution at a rotating speed of 1600 rpm of FeNi@NDC, FeCo@NDC, Fe@NDC and Pt/C. Neutral ZAB performance of FeNi@NDC. (b) Discharging polarization curves and corresponding power density plots. (c) Charge/discharge cycle stability of neutral liquid ZAB based on FeNi@NDC at 1 mA/cm^2.

covery characteristics. The Fig. 3c shows that the maximum power density provided by the FeNi@NDC (93.01 mW/cm^2) based ZAB is slightly higher than that of the Pt/C + RuO_2 (77.86 mW/cm^2) based ZAB. Fig. S10 (Supporting information) shows FeNi@NDC based ZAB has a smaller charge/discharge differential than Pt/C + RuO_2 based ZAB.

At the same time, FeNi@NDC delivers a discharge capacity of 761.3 mAh/g, slightly higher than that of the Pt/C + RuO_2 (727.5 mAh/g) (Fig. 3d). To demonstrate the stability of the ZAB, galvanostatic charge–discharge test was carried out at a current of 5 mA/cm^2 and each cycle is discharged for 10 min and then charged for 10 min, as shown in Fig. 3e. The voltage differences between charging and discharging of the battery is 1.03 V for approximately 115 h (345 cycles) of stable operation, which is better than the stability of the Pt/C + RuO_2 (Fig. S11 in Supporting information). To investigate the application of FeNi@NDC catalyst is further assembled into flexible ZABs and exhibit good open-circuit voltage and stability at 2 mA/cm^2, reflecting its potential practical application prospect in flexible energy storage devices (Figs. S12a–c in Supporting information).

To demonstrate the advantages of using neutral electrolytes, a neutral ZAB with NH_4Cl and KCl as the electrolyte is assembled. First, the FeNi@NDC catalytic activity of ORR is evaluated under neutral electrolyte (PBS, pH 7.4). The electrocatalytic ORR activities of all the catalysts were further investigated by LSV tests. As presented in Fig. 4a, $E_{1/2}$ of FeNi@NDC is 0.66 V, which is close to the catalytic performance of the noble metal catalyst ($E_{1/2}$, 0.71 V) and higher than the half–wave potentials of Fe@NDC ($E_{1/2}$, 0.51 V) and FeCo@NDC ($E_{1/2}$, 0.59 V). Due to the excellent ORR catalytic activity of the FeNi@NDC cathode in a neutral electrolyte, FeNi@NDC neutral ZAB is further assembled with an open circuit voltage of 1.21 V. Fig. 4b shows that the battery achieves a maximum power density of 31.44 mW/cm^2, which is better than Pt/C + RuO_2 (19.74 mW/cm^2). Moreover, such neutral ZABs display longer cycle stability (275 h) than alkaline batteries and similar charge/discharge voltage differences (Fig. 4c), and can be used as environmentally friendly energy devices with low current/power density requirements [20].

In summary, we have prepared an efficient bifunctional electrocatalyst by using waste leather and metal salts. Leather is rich in nitrogen and carbon; therefore, no additional heteroatomic precursors are needed, which reduces the production cost of the catalyst. The catalyst is analyzed from both physical and electrochemical perspectives. The alloy nanoparticles of the catalysts are anchored and distributed on a carbon substrate with numerous micropores and large specific surface areas. Due to the synergistic effect of the FeNi alloy and carbon substrate, FeNi@NDC exhibits good catalyst performances with a half-wave potential of 0.77 V and $E_{j\ =\ 10} = 1.66$ V. FeNi@NDC catalysts can be successfully used as cathode catalysts for alkaline and neutral ZABs. The peak power density of the assembled alkaline ZABs is 93.01 mW/cm^2, which is even better than that of commercial Pt/C. A charge–discharge cycle stability of 275 h is achieved with neutral ZABs. This work demonstrates the conversion of leather waste into iron-nickel alloy porous carbon material as a cost-effective and efficient bifunctional catalyst for applications in alkaline and neutral ZABs.

Declaration of competing interest

The authors declare that they have no known competing financial interests or personal relationships that could have appeared to influence the work reported in this paper.

Acknowledgment

This work was supported by National Natural Science Foundation of China (No. 22075139).

Supplementary materials

Supplementary material associated with this article can be found, in the online version, at doi:10.1016/j.cclet.2022.107756.

References

[1] S.S. Sekhon, J. Lee, J.S. Park, J. Energy Chem. 65 (2022) 149–172.
[2] Z. Bi, Q. Kong, Y. Cao, et al., J. Mater. Chem. A 7 (2019) 16028–16045.
[3] P. Liu, Z. Xing, X. Wang, et al., J. Mater. Sci. Mater. Electron. 33 (2022) 4887–4901.
[4] M. Sathish, B. Madhan, J. Raghava Rao, Waste Manag. 87 (2019) 357–367.
[5] M. Ayele, D.Y. Limeneh, T. Tesfaye, et al., Adv. Mater. Sci. Eng. 2021 (2021) 1–15.
[6] Y. Liu, X. Zhang, X. Gu, et al., Micropor. Mesopor. Mater. 303 (2020) 110303.
[7] R. Soni, S.N. Bhange, S. Kurungot, Nanoscale 11 (2019) 7893–7902.
[8] T. Zhou, N. Zhang, C. Wu, Y Xie, Energy Environ. Sci. 13 (2020) 1132–1153.
[9] Q. Zhou, Z. Zhang, J. Cai, et al., Nano Energy 71 (2020) 104592.
[10] L. Peng, L. Shang, T. Zhang, G. Waterhouse, Adv. Energy Mater. 10 (2020) 2003018.
[11] K. Wang, Z. Wang, Y. Liu, et al., Chem. Eng. J. 427 (2022) 131966.
[12] R. Xu, X. Wang, C. Zhang, et al., Chem. Eng. J. 433 (2022) 133685.
[13] S. Clark, A.R. Mainar, E. Iruin, et al., J. Mater. Chem. A 7 (2019) 11387–11399.
[14] T. Zhang, S. Zhang, S. Cao, Q. Yao, J. Lee, Energy Storage Mater. 33 (2020) 181–187.
[15] L. An, Z. Zhang, J. Feng, et al., J. Am. Chem. Soc. 140 (2018) 17624–17631.
[16] Y. Liang, H. Lei, S. Wang, Z. Wang, W. Mai, Sci. China Mater. 64 (2021) 1868–1875.
[17] Y. Chen, W. Zhang, Z. Zhu, et al., J. Mater. Chem. A 8 (2020) 7184–7191.
[18] T. Li, X. Peng, P. Cui, et al., SmartMat 2 (2021) 519–553.
[19] Y. Tian, L. Xu, J. Qian, et al., Carbon 146 (2019) 763–771.
[20] Y. Tian, X. Liu, L. Xu, et al., Adv. Funct. Mater. 31 (2021) 2101239.
[21] Y. Li, K. Xiao, C. Huang, et al., Nano-Micro Lett. 13 (2021) 1.
[22] W.Z. Cheng, J.L. Liang, H-B. Yin, et al., Rare Met. 39 (2020) 815–823.
[23] P. Tian, Y. Wang, W. Li, et al., J. Catal. 382 (2020) 109–120.
[24] M. Wu, G. Zhang, Y. Hu, et al., Carbon Energy 3 (2020) 176–187.
[25] C. Lai, X. Liu, C. Cao, et al., Carbon 173 (2021) 715–723.
[26] F. Dong, M. Wu, Z. Chen, et al., Nano-Micro Lett. 14 (2021) 36.
[27] X.R. Wang, J.Y. Liu, Z.W. Liu, et al., Adv. Mater. 30 (2018) e1800005.
[28] X. Zheng, X. Cao, K. Zeng, et al., Small 17 (2021) e2006183.
[29] Z. Wang, J. Ang, J. Liu, et al., Appl. Catal. B: Environ. 263 (2020) 118344.
[30] K. Chen, S. Kim, R. Rajendiran, et al., J. Colloid Interface Sci. 582 (2021) 977–990.
[31] T. Jiang, H. Hu, F. Lei, et al., ACS Appl. Mater. Interfaces 12 (2020) 38031–38044.
[32] G. Fu, Y. Chen, Z. Cui, et al., Nano Lett. 16 (2016) 6516–6522.
[33] Y. Zhou, B. Tang, S. Wang, et al., Int. J. Hydrog. Energy 45 (2020) 15785–15795.
[34] Y. Zhao, H.M. Zhang, Y. Zhang, et al., J. Power Sources 434 (2019) 226717.